

Research Article

Structural insights into the mechanism of oxidative activation of heme-free H-NOX from *Vibrio cholerae*

Roma Mukhopadhyay¹, Kelly N. Chacón², Jacqueline M. Jarvis³, Marat R. Talipov¹ and  Erik T. Yuki¹

¹Department of Chemistry and Biochemistry, New Mexico State University, Las Cruces, NM 88003, U.S.A.; ²Department of Chemistry, Reed College, Portland, OR 97202, U.S.A.; ³Department of Plant and Environmental Sciences, New Mexico State University, Las Cruces, NM 88003, U.S.A.

Correspondence: Erik T. Yuki (etyuki@nmsu.edu)



Bacterial heme nitric oxide/oxygen (H-NOX) domains are nitric oxide (NO) or oxygen sensors. This activity is mediated through binding of the ligand to a heme cofactor. However, H-NOX from *Vibrio cholerae* (*Vc* H-NOX) can be easily purified in a heme-free state that is capable of reversibly responding to oxidation, suggesting a heme-independent function as a redox sensor. This occurs by oxidation of Cys residues at a zinc-binding site conserved in a subset of H-NOX homologs. Remarkably, zinc is not lost from the protein upon oxidation, although its ligation environment is significantly altered. Using a combination of computational and experimental approaches, we have characterized localized structural changes that accompany the formation of specific disulfide bonds between Cys residues upon oxidation. Furthermore, the larger-scale structural changes accompanying oxidation appear to mimic those changes observed upon NO binding to the heme-bound form. Thus, *Vc* H-NOX and its homologs may act as both redox and NO sensors by completely separate mechanisms.

Introduction

The bacterial heme nitric oxide/oxygen (H-NOX) protein family was identified in 2003 through homology to the heme-binding domain of soluble guanylate cyclase (sGC) [1]. In mammals, sGC acts as a nitric oxide (NO) sensor, increasing levels of the secondary messenger cyclic GMP in response to NO binding to the heme iron [2]. Bacterial H-NOX proteins also bind heme and can be functionally divided into two groups based on the lifestyle of bacteria from which they originate [3]. Those found in strict anaerobes form stable Fe(II)-O₂ species. They are fused to methyl-accepting chemotaxis proteins (MCP) and likely mediate chemotaxis in response to O₂. Like sGC, the H-NOX proteins from facultative anaerobes do not stably bind O₂. They modulate the activity of histidine kinases (HK) or H-NOX-associated cyclic-di-GMP processing enzymes (HaCE) in a NO-dependent manner, regulating biofilm formation [4–7], symbiont/host colonization [8] or quorum sensing [9].

One of the best-studied H-NOX/HK NO signaling systems comes from *Shewanella oneidensis*. Elegant phosphotransfer profiling experiments elucidated the signaling pathway beginning with autophosphorylation of the HK HnoK [6]. HnoK then phosphorylates the *c*-di-GMP phosphodiesterase HnoB, activating it to hydrolyze *c*-di-GMP and inhibit biofilm formation. H-NOX in the Fe(II)-NO state strongly inhibits HnoK autophosphorylation [10], resulting in an increase in cyclic-di-GMP levels and biofilm formation in response to NO. This signaling system is conserved in *Vibrio cholerae*, and autophosphorylation of *Vc* HnoK and phosphotransfer to response regulators has been confirmed [6].

As for *S. oneidensis*, holo *Vc* H-NOX in both Fe(III) and Fe(II)-NO states is a potent inhibitor of *Vc* HnoK autophosphorylation [11]. However, Fe(II) *Vc* H-NOX reacts with O₂ [12], and the heme is sensitive to degradation in the presence of excess reductant and air [11]. Unexpectedly, the heme-free form is also a good inhibitor of HnoK autophosphorylation when reversibly activated by oxidation by hypochlorous acid (HOCl). The mechanism involves the oxidation of 4 Cys residues to form disulfide bonds. Based on homology with *S. oneidensis* H-NOX, three of these Cys co-ordinate a zinc ion along with a

Received: 6 February 2020
Revised: 3 March 2020
Accepted: 6 March 2020

Accepted Manuscript online:
6 March 2020
Version of Record published:
23 March 2020

Gln residue in the reduced state. Remarkably, although the oxidized Cys residues are no longer able to co-ordinate zinc, metal is stoichiometrically retained by the protein after oxidation and buffer exchange. This led to the hypothesis that disulfide bond formation causes a change of zinc ligation, either or both of which may be important to mediate the conformational change that activates *Vc* H-NOX to bind and inhibit *Vc* HnoK.

Here, we have performed an analysis of H-NOX sequences to identify the conservation and diversity of putative sulfur-ligated zinc sites. We have also defined the mechanism of oxidative activation of *Vc* H-NOX, using computational methods to evaluate possible zinc coordination environments and disulfide bonding patterns in the reduced and oxidized states. These models are complemented by extended X-ray absorption fine structure (EXAFS) and mass spectrometry experiments defining the zinc ligation environment and disulfide bonding pattern, respectively. The results from computational and experimental methods are consistent and provide conclusive evidence that oxidant sensing in heme-free H-NOX proceeds via specific disulfide bond formation and reorganization of the zinc site. A comparison of the overall structural changes likely accompanying oxidation with those observed on NO binding to the heme-bound protein [13] reveal similarities that may explain how *Vc* H-NOX is able to interpret these disparate chemical signals.

Materials and methods

Phylogenetic analysis of H-NOX

The protein sequence of *Vc* H-NOX (UniProtKB accession number Q9KLM3) was used to perform a BLAST search of the UniProtKB database [14]. Sequences were filtered to include only those with *E*-values below 10^{-20} . These sequences were submitted to the Enzyme Function Initiative — Enzyme Similarity Tool [15–17] to generate a sequence similarity network (SSN), which was further processed and visualized in Cytoscape [18]. Sequences were aligned using Clustal Omega [19].

Conventional molecular dynamics (cMD)

The initial structure of *Vc* H-NOX [11] for MD simulation was generated by SwissProt [21] software from the X-ray crystal structure of *S. oneidensis* (So) H-NOX (PDB id: 4U99), as described in ref. [13]. MD simulations were done with the AMBER 16 package [22] using ff14SB force field [23]. The side chains of the aspartate and glutamate amino acids were in the deprotonated form in the MD simulation, and the histidine imidazoles were protonated only at the N ϵ atom (see additional information in Supplementary Table S1). Cysteine amino acids were in their anionic forms in the models of reduced H-NOX. For the partially and fully oxidized H-NOX models, disulfide bonds were added using the harmonic constraints on the sulfur atoms of cysteine residues. The cMD simulations have been performed using graphical processing units (GPU) [24,25]. Periodic boundary conditions were used in the MD simulations with cubic cell and a distance between any protein atom and cell boundary of at least 10 Å. Particle Mesh Ewald (PME) summation [26] was used to calculate the long-ranged electrostatic interactions with the cut-off distance of 10 Å. The protein structures were solvated by explicitly presented TIP3P water molecules [27,28]. Counter-ions (Na⁺) were added to neutralize the overall charge of the periodic cell. Time step of 4 fs was used in combination with the hydrogen mass repartitioning (HMR) [29–31] and SHAKE algorithms [32]. The SHAKE algorithm was used to restrain only the bonds containing hydrogen atoms.

Initial minimization was done with restraints on the protein atom positions for 1000 steps and then a minimization was done without restraints for 2500 steps. Then the system temperature was linearly increased using isothermal-isochoric ensemble (NVT) for 400 ps from 0 to 300 K and then equilibrated for 1 ns using isothermal-isobaric (NPT) ensemble. Finally, simulations were done in triplicates for at least 400 ns for each trajectory using the NPT ensemble. The resulting structures generated from simulations were viewed using visual molecular dynamic (VMD) software [33]. Root-mean-square difference (RMSD) analysis was performed using the least squared fitting of all the atoms of the protein backbone.

Molecular mechanics combined with generalized Born solvation surface area approach (MM/GBSA)

The MM/GBSA method was used to compare the relative free energy between specific conformations for reduced, partially oxidized and oxidized H-NOX models by using 6000 snapshots from each MD trajectory. The water molecules and the counter-ions were removed from the produced snapshot structures. The obtained de-solvated protein structures were subjected to the potential energy evaluation using implicit solvation model

within the generalized Born (GB) approximation. The calculations were performed with the pairwise GB model by Hawkins et al. [34,35], with the parameters proposed by Tsui and Case [36] and the effective salt concentration of 0.01 M.

Umbrella sampling

Umbrella sampling [37] is a biasing sampling method used to improve the sampling of a system by monitoring the evolution of canonical MD simulation along a certain degree of freedom. Umbrella sampling for reduced H-NOX model was done by following the distance between zinc cation and the surrounding residues. A series of 27 simulation ‘windows’ were introduced for the distance between zinc and residue of interest from 1.8 to 7 Å with the step size of 0.2 Å (see Supplementary Tables S2–S8). A harmonic biasing potential of 50 kcal/(mol-Å²) was applied to each of the distances between the zinc and the residue of interest. Up to 17 additional sampling windows were added in case of insufficient overlap between the individual histograms for better sampling efficiency. The Newton–Raphson-based method was used for solving the weighted histogram analysis method (WHAM) equations [38].

Fragment molecular orbital method/density functional tight binding (FMO/DFTB3)

Quantum mechanical (QM) method DFTB3 was applied using FMO code distributed in the US Gamess package [39,40]. FMO [41,42] was used to calculate energy and energy gradient faster than traditional QM methods by dividing large molecular systems into small fragments and implementing self-consistent density functional calculations of the fragment monomers and dimers. The fragments of the proteins were generated using the software Facio [43–46] by cleaving the protein backbone in between the C and C^α atoms in such a way that each fragment contained two neighboring amino acids with the exception of disulfide bridges whose fragments contained four amino acids. The polarized continuum model (PCM) was used to take the solvation effects into account [47]. The convergence criterion for the self-consistent charge field chosen was 10⁻⁹ a.u. For the FMO/DFTB3 calculations, 108 snapshots, evenly distributed along the MD simulation course, were used. The resulting distributions of the electronic potential energies for the partially oxidized H-NOX models were plotted as probability density plots using R platform [48,49] and Jupyter notebook [50,51].

Expression and purification of proteins

Full-length, untagged, heme-free Vc H-NOX was expressed from BL21 *Escherichia coli* cells and purified by anion exchange and size exclusion chromatography as previously described [11]. Protein was stored in HEPES storage buffer (50 mM HEPES pH 8.0, 300 mM NaCl, 5% glycerol).

Extended X-ray absorption fine structure (EXAFS)

Reduced WT Vc H-NOX was generated by incubating 1.3 ml of protein at 300 μM with 5 mM DTT in HEPES storage buffer for 30 min on ice and desalting into HEPES storage buffer using a 5 ml HiTrap[®] desalting column (GE Healthcare). The oxidized protein was generated by incubating 91.6 μM of the reduced and desalted protein with 1 mM HOCl for 1 h at room temperature followed by desalting as above. The samples were concentrated to ~100 μl using centrifugal filtration devices (Millipore) resulting in final concentrations for reduced and oxidized samples of 1.35 mM and 0.93 mM, respectively. Ninety microliters of protein or buffer was combined with 10 μl ethylene glycol, loaded into EXAFS cuvettes and flash frozen in liquid nitrogen.

X-ray absorption data were collected at the Stanford Synchrotron Radiation Lightsource. Extended X-ray absorption fine structure (EXAFS) of Zn (9658 eV) was measured on beamlines 9–3 and 7–3 in duplicate when available using a Si 220 monochromator with crystal orientation $\varphi = 0^\circ$ to reduce the likelihood of known crystal glitches in the Zn energy range. Samples were measured as frozen aqueous glasses in 10% ethylene glycol at 15 K, and the X-ray absorbance was detected as K α fluorescence using either a 100-element (beamline 9–3) or 30-element (beamline 7–3) Canberra Ge array detector. A Z-1 metal oxide filter (Cu) and Soller slit assembly was placed in front of the detector to attenuate the elastic scatter peak. Four to six scans of a buffer blank were measured at the absorption edge and subtracted from the raw data to produce a flat pre-edge and eliminate residual Cu K β fluorescence of the metal oxide filter. Energy calibration was achieved by placing a Zn metal foil between the second and third ionization chamber. Data reduction and background subtraction were performed using EXAFSPAK [52]. The data from each detector channel were inspected for drop outs and

glitches before being included into the final average. EXAFS simulation was carried out using the program EXCURVE 9.2 as previously described [53–55].

Trypsin digest and mass spectrometry

Fully reduced H-NOX was generated by incubating 250 μ M protein with 5 mM DTT in HEPES storage buffer for 30 min at room temperature. DTT was then removed by desalting using Zeba™ spin desalting columns (Pierce). Oxidized protein was generated by incubating 150 μ M reduced and desalted protein with 1.5 mM HOCl in HEPES storage buffer followed again by desalting. N-ethyl maleimide (NEM) and guanidinium-HCl were added to 4 mM and 6 M, respectively, and samples heated to 37°C for 1 h. Samples were diluted with dI water and concentrated buffer to reach a final concentration of 1 M guanidinium-HCl, 50 mM Tris pH 8.0, 20 mM CaCl₂. Trypsin-ultra™ (New England Biolabs) was added at a mass ratio of 1 : 50 and incubated at 37°C overnight. The digest was quenched by the addition of formic acid to 1% v/v. Samples were passed through a 0.2 μ m filter prior to injection onto a C18 column (Sunfire 3.5 μ m, 3 \times 150 mm) connected to a HPLC system (Agilent). A gradient of 5–55% acetonitrile with 0.1% formic acid was applied over 40 min at 0.5 ml/min and 0.5 ml fractions were collected. Fractions with low abundance peptides were dried under a stream of nitrogen gas and reconstituted in 50 μ l of 50% acetonitrile, 0.1% formic acid.

Samples were directly infused using an automated electrospray ionization (ESI) robot (Advion Nanomate) coupled to an Orbitrap Fusion mass spectrometer. An instrument method was created to automatically collect data-dependent tandem MS spectra for the peptide of interest. Positive-ion broadband ESI spectra (5 microscans) were collected from m/z 375 to 2000 at a resolving power of 120 000 at m/z 200 and AGC target of 400 000. The ions of interest, m/z 989.24 (+4 charge state), were selected for fragmentation using EThcD with the following conditions: quadrupole isolation window = 1.6, 50 ms reaction time, reagent target = 1 000 000, max reagent injection time = 200 ms, 25% supplemental activation collision energy, AGC target = 10 000, max injection time = 200 ms and ion trap detection of single microscans. MS³ spectra were collected from the fragmentation of the product ions from the MS² spectra using the following conditions: quadrupole isolation = 2.5, MS² mass isolation window = m/z 2, HCD activation at 29–29.5% collision energy, AGC target = 10 000, max injection time = 200 ms and ion trap detection of 10 microscans.

Results

Conservation of zinc-binding sites

It was previously noted that the three zinc-binding Cys residues identified in *S. oneidensis* (Cys139, Cys164 and Cys172) were conserved among roughly half of the available *hnox* sequences from gammaproteobacteria where the fourth ligand (His161) is conserved as either Gln or His [13]. To analyze the degree of conservation of potential zinc-binding sites, a BLASTP search was performed using the *Vc* H-NOX sequence. 598 sequences were identified with a BLAST score of $\leq 10^{-20}$ that fall into four main groups based on a SSN (Figure 1A). The proximal His ligand to the heme (His103 in *S. oneidensis*) is absolutely conserved across all sequences. Group 1 is composed of sequences from diverse species and there is no indication of a conserved Cys-ligated zinc site (Figure 1B). Group 2 is predominantly composed of sequences from gammaproteobacteria including *S. oneidensis* and *V. cholerae*. Here the 3 Cys ligands to zinc are very highly conserved, and the fourth ligand to zinc in *S. oneidensis* (His161) is conserved as either His or Gln. Interestingly, this is also true of sequences from group 3, even though only a few sequences derive from gammaproteobacteria, suggesting that zinc coordination by H-NOX proteins is not confined to this bacterial class. Finally, group 4 is composed entirely of gammaproteobacteria from the *Vibrio* and *Photobacteria* genera. While the Cys residues from groups 2 and 3 are not conserved in group 4, a distinct pattern of 3 Cys residues is very highly conserved in this group. To date, none of these proteins have been characterized *in vitro*, so it will be of interest to determine whether these may also bind zinc or another metal through this Cys motif.

To estimate the zinc-binding environment of *Vc* H-NOX, we previously generated a homology model using the homolog from *S. oneidensis* [11], its closest structurally characterized relative. Apart from the expected apparent coordination by Cys149, Cys172, Cys182 and Gln171, a large number of potential metal-binding residues were also identified (Figure 1C). None are highly conserved. Nevertheless, they were systematically mutated to Ala in order to determine whether any may have a role in zinc coordination, particularly when the Cys ligands are oxidized. In addition to the previously described C177A mutant, only H176A was found to be expressed in soluble form in *E. coli*. H176A *Vc* H-NOX was very similar to WT in terms of zinc quantitation,

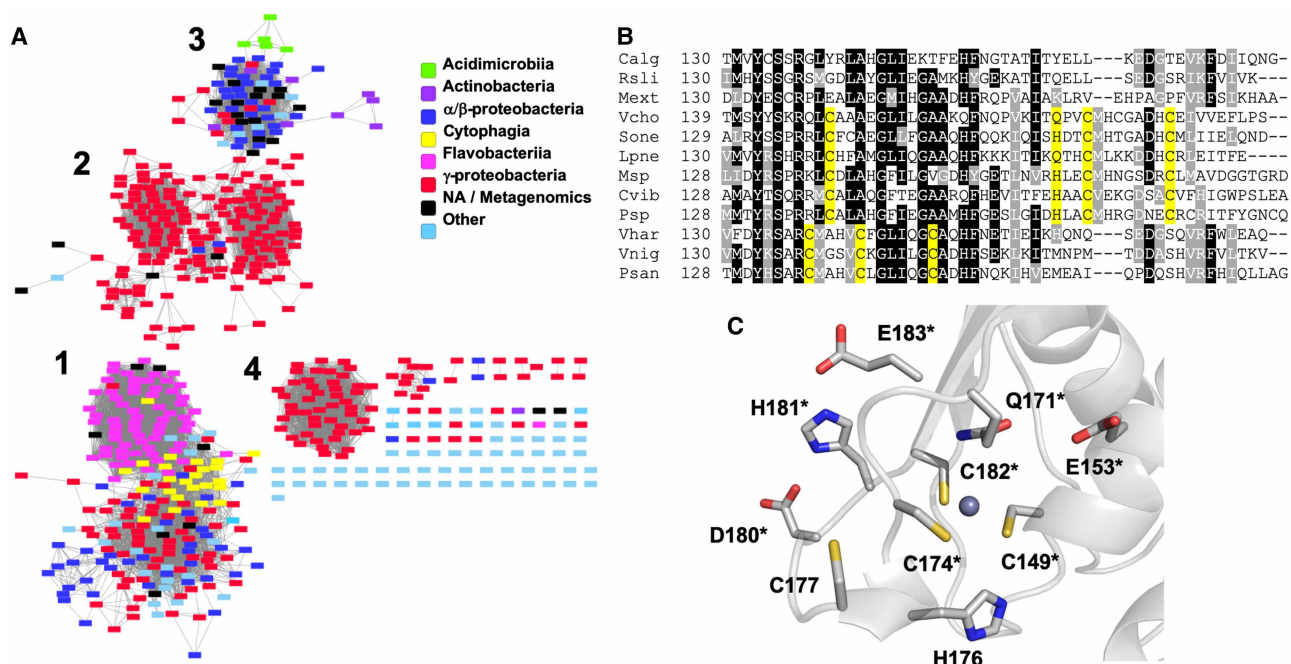


Figure 1. Conservation of zinc binding sites among H-NOX homologues.

(A) Sequence similarity network including 599 sequences filtered such that only edges associated with E -values less than 10^{-47} are included in the network. Sequences are represented by rectangles colored according to class. (B) Multiple sequence alignment of three representative sequences from each group in (A). Putative zinc-binding residues are highlighted in yellow. Species names are abbreviated as follows: (Group 1) *Calg*, *Cellulophaga algicola*; *Rsl1*, *Runella slithyformis*; *Mext*, *Methylobacterium extorquans*; (Group 2) *Vcho*, *Vibrio cholerae*; *Sone*, *Shewanella oneidensis*; *Lpne*, *Legionella pneumophila*; (Group 3) *Msp*, *Mycobacterium sp.*; *Cvib*, *Caulobacter vibrioides*; *Psp*, *Pseudomonas sp. DY-1*; (Group 4) *Vhar*, *Vibrio harveyi*; *Vnig*, *Vibrio nigripulchritudo*; *Psan*, *Photobacterium sanguinicancri*. (C) Zinc coordination environment in a *Vc* H-NOX homology model. Each of the residues in the figure has been mutated to Ala and those indicated by asterisks result in insoluble protein.

Cys oxidation and reversible HnoK inhibition (Supplementary Figure S1). Thus, His176 does not appear to have a major role in zinc coordination or redox sensing. While the role of the other residues is uncertain due to insolubility of the mutants, this result does illustrate that protein stability is very sensitive to mutations of potential metal-ligand residues at the zinc-binding site.

Computational modeling: reduced H-NOX

The homology model of the reduced *Vc* H-NOX zinc site [11], further referred to as **R1**, was used as the starting point for classical molecular dynamics (cMD) simulations. An MD simulation of this model was run in triplicate for 7.8 μ s resulting in a total 23.4 μ s simulation. The microsecond-scale simulations showed that **R1** was kinetically stable, as the zinc cation remained co-ordinated with Cys149, Cys174, Cys182 and Gln171 throughout the entire simulation, and the positions of backbone atoms were nearly invariant over time (RMSD < 2.7 Å).

It might seem surprising that zinc cation is co-ordinated with Gln171 rather than His176 or His181 in the **R1** model since histidine residues are more common zinc ligands than glutamine. To explore whether zinc cation can bind with nearby histidine residues, we performed cMD simulations of the formation of zinc complexes with His176 or His181 using a temporarily enabled biasing harmonic potential to bring zinc and histidine into close proximity. The subsequent simulations with removed biasing potential led to a fast dissociation of the His176/Zn bonding within the 1.3 μ s simulation (**R2**) and of the His181/Zn bonding within 400 ns simulation (**R2'**). This observation suggests that His/Zn complexes in *Vc* H-NOX were kinetically unstable, particularly **R2'**, which was consequently excluded from further analysis. A subsequent comparison of the thermodynamic stability of the **R1** and **R2** models, performed using the MM/GBSA analysis, showed that model **R1** was lower in potential energy by 4.8 ± 0.4 kcal/mol than **R2**, thus suggesting that Gln171 is a thermodynamically more favorable ligand than His176 (Supplementary Figure S2).

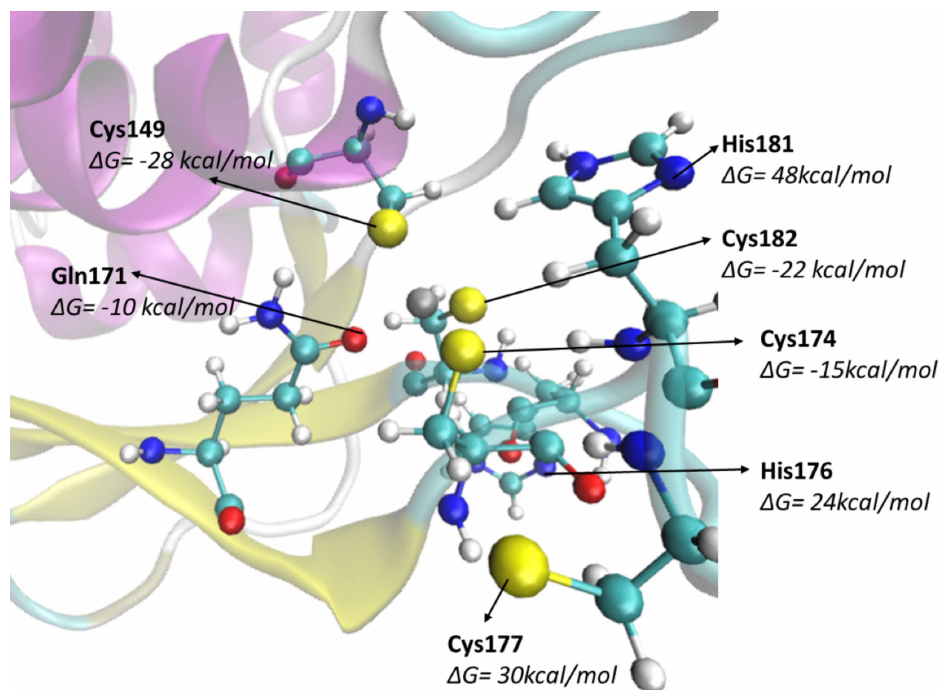


Figure 2. The fully reduced Vc H-NOX zinc binding site.

(A) Zinc site of the thermodynamically and kinetically stable form of reduced H-NOX **R1** with the residues near zinc site and the corresponding free energy required for the residues to interact with zinc.

To solidify the results obtained from the MM/GBSA analysis on the thermodynamic stability of **R1**, a free energy profile of the formation of the bond between the zinc cation and its ligand was constructed using the umbrella sampling technique. The distance between zinc and the residue of interest was taken as the reaction coordinate to plot the potential of mean force (PMF) diagram (Supplementary Figure S3). The computed PMF plots demonstrated that zinc binds exothermically to Cys174 ($\Delta G = -15$ kcal/mol), Cys149 (-28 kcal/mol), Cys182 (-22 kcal/mol) and Gln171 (-10 kcal/mol) but not with Cys177 ($\Delta G = +30$ kcal/mol), H176 ($+24$ kcal/mol) or H181 ($+48$ kcal/mol). Thus, the cMD simulations, MM/GBSA results and umbrella sampling PMF plots for reduced H-NOX strongly indicated that zinc in reduced H-NOX was co-ordinated by Cys149, Cys174, Cys182 and Gln171 amino acid side chains (Figure 2).

Computational modeling: partially oxidized H-NOX

In Vc H-NOX, three cysteine residues that directly interact with zinc and one additional cysteine (Cys177) in proximity to the zinc-binding site are present. Partial oxidation of Vc H-NOX can produce a single disulfide bond between two cysteines, however, the identity of these cysteines involved in the disulfide bonds for the partially or fully oxidized H-NOX was not known. Combination of all possible cysteine residues to form a single disulfide bond generated six different models of partially oxidized H-NOX (**P1**, **P1'**, **P2**, **P2'**, **P3** and **P3'**) (Table 1). The MD simulations showed that all of these models were kinetically stable for the entire simulation range of 1.2 μ s (RMSD < 3.4 Å). The following MM/GBSA analysis showed that model **P1'** was the most stable one while models **P3** and **P3'** could be excluded from further consideration because of the obvious energetic penalty (Table 1).

The MM/GBSA results, presented above, include only coulombic and van der Waals terms and neglect any contributions from the zinc-based orbital interactions. To take the orbital interactions into account, we used a QM approach FMO/DFTB3, as described in the computational methods. The distributions of the FMO/DFTB3 potential energies of the protein conformations during the MD simulation course confirmed that the Cys174/182 (**P1'**) bonding interaction was the most stable one while models **P2** and **P2'** were comparable in energy and at least 57 kcal/mol less stable than **P1'** (Figure 3). This result suggests that the formation of the bond

Table 1. Tabulated relative free energy ($\Delta\Delta G = \Delta G_{\text{calc}} - \Delta G_{\text{ref}}$) for various partially oxidized H-NOX models as computed by MM/GBSA. $\Delta G_{\text{ref}} = \Delta G_{\text{calc}}(\text{P1}')$

Model	Disulfide bridge	$\Delta\Delta G$ (kcal/mol)	Std. error
P1	Cys149–Cys177	26.5	1.2
P1'	Cys174–Cys182	0.0 (reference)	—
P2	Cys149–Cys182	37.4	0.1
P2'	Cys174–Cys177	8.7	0.1
P3	Cys149–Cys174	117.8	0.2
P3'	Cys177–Cys182	134.1	0.2

between Cys174 and Cys182 (that is, **R1** \rightarrow **P1'** transformation) represents the first oxidation event for reduced Vc H-NOX.

Computational modeling: fully oxidized H-NOX

Three different models of fully oxidized H-NOX could be combinatorially generated, that is model **O1** (Cys174/182 and Cys149/177 bonds), **O2** (Cys149/182 and Cys174/177 bonds) and **O3** (Cys149/174 and Cys177/182 bonds). The models **O1** and **O2** were subjected to a 1.2 μs simulations and were found to be kinetically stable (RMSD < 3.7 Å) while **O3** was discarded from further consideration as it would require a formation of highly energetically unfavorable Cys149/174 (**P3**) and Cys177/182 (**P3'**) interactions. The subsequent MM/GBSA analysis demonstrated that the model **O1** was energetically more favorable over **O2** by 16.6 ± 0.1 kcal/mol (Supplementary Figure S4). Thus, the computational modeling suggests that oxidation of Vc H-NOX leads to **P1'** (Cys174/182 bond) and, subsequently, **O1** (Cys174/182 and Cys149/177 bonds).

Our previous study indicated that fully oxidized H-NOX still retains the zinc cation [11]. However, its precise location and coordination environment in the oxidized state remains unknown. In the model **O1**, Zn was originally placed at the same position where it was in the reduced form of H-NOX. The cMD simulations showed that

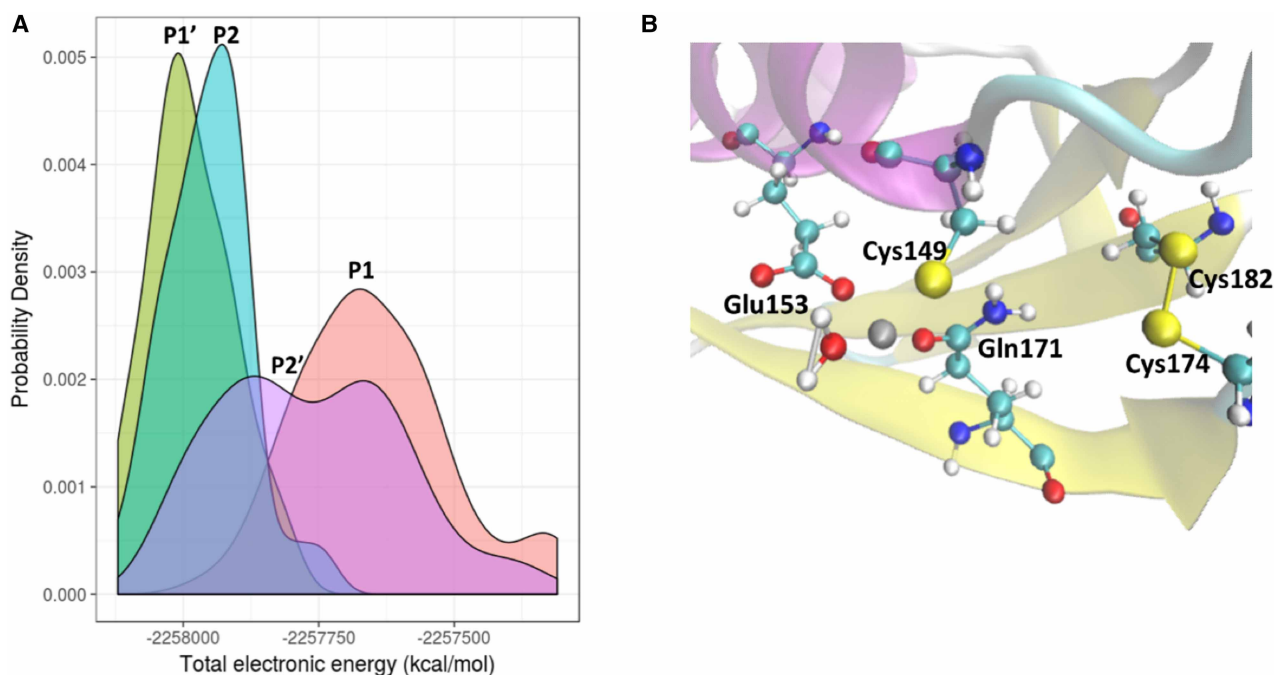


Figure 3. The partially oxidized Vc H-NOX zinc binding site.

(A) Probability density distribution from FMO/DFTB3 results show the bond energetics in different partially oxidized models. (B) Zinc site in partially oxidized H-NOX model **P1'**.

it resides in a loosely defined pocket containing the side chain of Glu153 and backbone carbonyls of Ile184, Thr170, Val185 and Ile169. To identify whether there existed other binding regions for the zinc cation, the electrostatic potential energy surface of the oxidized H-NOX model was analyzed using Chimera [56] software (Supplementary Figure S5). Based on this analysis, we generated a series of new models of oxidized H-NOX in which zinc was placed in the regions with prominent electron-deficient character. This resulted in 11 different models, which were subjected to the cMD simulations followed by MM/GBSA calculations. However, no well-defined zinc-binding pocket could be identified despite multiple attempts. Similar simulations, conducted for the O2 model, also showed a large variation of the zinc cation position. At the same time, the generated models were of higher energies as compared with O1 thus solidifying the conclusion that O1 indeed was more stable than O2.

Zinc EXAFS of reduced and oxidized Vc H-NOX

Zn K-edge EXAFS was employed to experimentally define the coordination environment of zinc in reduced and oxidized H-NOX. The Fourier transform (FT) of the reduced form (Figure 4A) shows a strong peak centered ~ 2.314 Å consistent with sulfur ligation, with a slight shoulder at 2.014 Å due to oxygen or nitrogen ligation. The simulated EXAFS of the reduced form (Figure 4A inset) fit remarkably well to the data and indicates 3 S and 1 O/N ligands (Table 2), consistent with model R1 (Figure 2) of H-NOX where Cys149, Cys174, Cys177 and Gln171 co-ordinate the zinc ion. Of note are the low Debye–Waller (DW) values for all four ligands, indicating that these residues do not exhibit notable flux upon binding of the metal ion. In contrast, the EXAFS of oxidized H-NOX (Figure 4B) was significantly different and exhibited weaker scattering atoms at shorter distances, which is consistent with a change from a primarily sulfur ligation sphere to one dominated by O/N ligands. Indeed, EXAFS simulations indicate a complete loss of sulfur ligation in favor of a new tetra or penta-co-ordinate environment. We are able to best fit to an environment composed of 4 O/N ligands at 1.955 Å with a fifth multiple scattering contribution at the same distance that was best modeled by a histidine. As the DW factor for the O/N ligands were unusually high for this type of scatterer (0.015 Å²), it is likely that the Zn associates flexibly with those atoms, which might be expected in order for the movement to occur from the reduced to the oxidized site. This flexibility may also indicate a more biologically typical tetraco-ordinate environment, which includes a stably associated histidine. While this coordination does not precisely match any of the zinc sites in modeled oxidized structures, the EXAFS data conclusively demonstrates a marked change in zinc coordination from primarily sulfur to primarily O/N upon oxidation. Desalting the oxidized sample into the fresh buffer prior to EXAFS data collection allows us to rule out contributions of any aquo- or buffer-zinc complex that might form as a result of dissociation from the protein, which was not observed to any significant degree in our previous study [11].

Mass spectrometry identification of the disulfide bonding pattern in oxidized Vc H-NOX

Our previous work combined with the above results demonstrates that oxidation results in complete loss of Cys ligation to the zinc and the formation of two disulfide bonds. Since 3 out of 4 Cys residues are housed on the

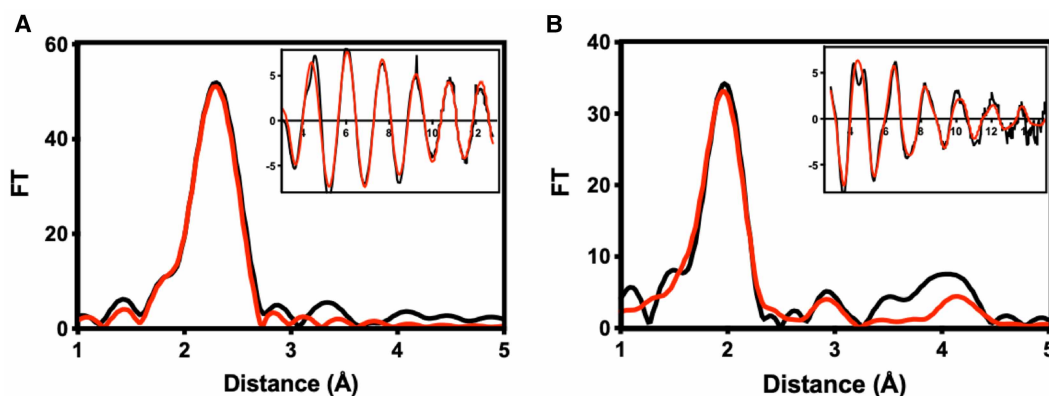


Figure 4. EXAFS spectra of fully reduced and fully oxidized Vc H-NOX.

Zn K EXAFS and Fourier transforms of reduced (A) and oxidized (B) H-NOX. Black traces represent experimental data and red traces are simulations. Parameters used to generate the simulated spectra are listed in Table 2.

Table 2. Fit parameters for Zn EXAFS simulations

	FI	No	<i>R</i> (Å)	DW (Å ²)	No	<i>R</i> (Å)	DW (Å ²)	No	<i>R</i> (Å)	DW (Å ²)	<i>E</i> ₀
Zn K		Zn-S			Zn-N/O			Zn-N(His)			
Red	0.27	3	2.314	0.004	1	2.014	0.002				−11.97
Ox	0.47				4	1.955	0.015	1	1.995	0.003	−11.37

same tryptic peptide, a tandem mass spectrometry (MS³) protocol similar to that previously published [57] was developed to determine the disulfide bonding pattern. The protocol employs electron transfer dissociation with supplemental high collision energy activation (ETHcD; MS²) and high collision-induced dissociation (HCD; MS³) to differentiate between intra- and inter-peptide disulfide bonds. ETD and the related electron capture dissociation (ECD) preferentially fragment disulfide bonds over peptide bonds [58–60]. Subsequent analysis of the resulting peptides by HCD fragmentation at peptide bonds by MS³ allows for their identification. Furthermore, since disulfide bonds are not typically fragmented by CID [61], no fragmentation is observed at residues within an intrapeptide disulfide. Similar approaches have been used to assign complex disulfide bonding patterns in antibodies [57,62–64]. Our approach depends on the ability to fragment the inter-peptide disulfide bond by ETHcD and select for the resultant fragment with the intrapeptide bond still intact for HCD-MS³. A window of residues between Cys residues will not fragment in the MS³ step and identify the cysteines involved in this bond.

In oxidized WT H-NOX, the cross-linked +4 parent ion with *m/z* = 989.24 was positively identified from offline HPLC fractions. Notably, this ion was not identified in reduced H-NOX mass spectra nor was its counterpart observed in oxidized C177A H-NOX. ETD fragmentation yielded two new peptides with masses consistent with Ile169-Ser191 (P1) and Gln147-Lys161 (P2) (Figure 5A), indicating that ETD ruptured the inter-peptide disulfide bond. These assignments were confirmed by HCD fragmentation (Figure 5B,C, Supplementary Tables S9,S10). Furthermore, the HCD fragmentation pattern of Ile169-Ser191 is consistent with an intra-disulfide bond between Cys174 and Cys182 as virtually no fragments are observed between these two residues. A possible b₁₃ fragment was identified, which would indicate cleavage between Cys182 and His181. However, the *m/z* is 1 unit larger than expected for this fragment, even assuming all Cys residues are protonated (Supplementary Table S10). It is possible that this is due to a small amount of P2 peptide with both disulfide bonds severed during ETHcD fragmentation. Alternatively, it may be due to neutral loss from an unidentified c, z, y, or b-ion. In any case, no other y- or b-ions for fragments between Cys174 and Cys182 could be identified. Taken together, the mass spectrometry data strongly suggests that the disulfide bonding pattern in oxidized H-NOX is between Cys174–Cys182 and Cys177–Cys149 as indicated in Figure 5A and predicted computationally (Supplementary Figure S4).

Discussion

Structural studies on the H-NOX family have made significant progress toward understanding the mechanisms of signal transduction [65]. Briefly, NO binding to the heme iron displaces the proximal His ligand, relieving heme distortion imposed by steric constraints with a conserved, proximal Pro residue. The displaced proximal His rotates out of the pocket ~90° along with helix αF. These perturbations lead to a small rigid-body displacement and rotation of the distal subdomain relative to the proximal subdomain. The rotation occurs about a hinge composed of two conserved Gly residues (G81 and G154 in *Vc* H-NOX). While the initial events differ between NO and O₂ sensing H-NOX proteins, Pro-heme interactions and subdomain realignment appear to be conserved, at least between the NO-sensing H-NOX from *S. oneidensis* [13,66] and the O₂-sensing H-NOX from *Caldanaerobacter subterraneus* [67–70]. Hydrogen-deuterium exchange mass spectrometry (HDX-MS) experiments indicate that *So* H-NOX [71] and *Vc* H-NOX [72] interact with their respective histidine kinases (HnoK) through the distal subdomain helices αA–αC and proximal subdomain helix αF. This supports the idea that reorientation of subdomains modulates the interaction between H-NOX and HnoK, mediating autokinase inhibition in the presence of the appropriate signal.

Intriguingly, a comparison of the lowest energy models of reduced and oxidized heme-free apo H-NOX reveal significant changes at αA–αC, αF and the glycine hinge region (Figure 6A). In this case, these motions

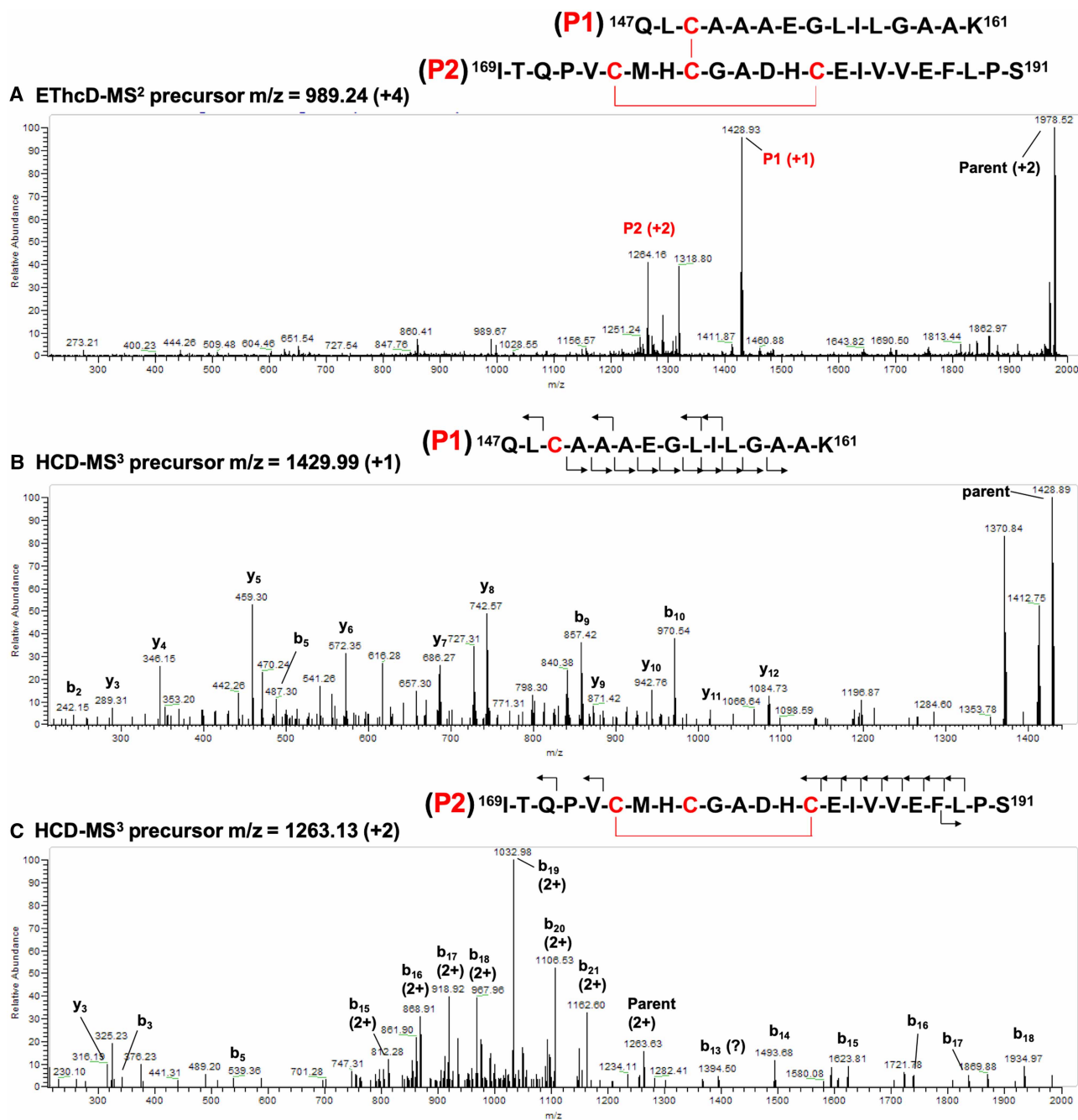


Figure 5. Mass spectra of the disulfide cross-linked peptide of oxidized H-NOX.

(A) ETHcD-MS² spectrum of m/z 989.24 (+4). (B) HCD-MS³ spectra of the P1 peptide with m/z 1429.99 (+1) and (C) the P2 peptide with m/z 1263.13 (+2). The peptide sequences with the observed fragment ions are shown above each spectrum with Cys residues and disulfide bonds indicated in red.

are likely mediated by the impact of disulfide bond formation on the nearby glycine hinge (Figure 6B). In particular, C149 must move $\sim 5 \text{ \AA}$ to form a disulfide bond with C177. The position of C149 at the N-terminal end of αG only 5 residues from G154 suggests that this motion will be communicated to the glycine hinge, promoting reorientation of the subdomains. Based on these models and our previous biochemical data, it seems likely that disulfide bond formation in heme-free H-NOX may mimic motions accompanying NO binding to the heme iron, resulting in a conformation of H-NOX capable of inhibiting HnoK autophosphorylation.

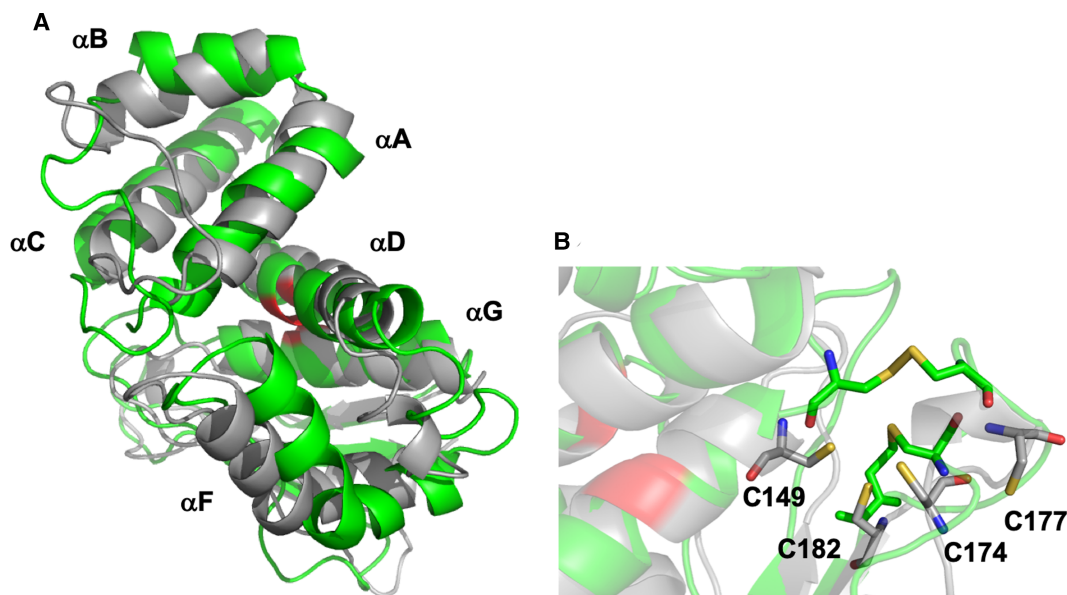


Figure 6. Models of heme-free reduced (gray) and oxidized (green) *Vc* H-NOX.

(A) Overall structures showing positions of important alpha helices. (B) Reduced zinc-binding site. Zinc has been omitted for clarity. Cys residues are shown as sticks colored according to element. Gly81 and Gly154 at the glycine switch are colored red.

The reversible formation of disulfide bonds at Cys-ligated zinc sites is proposed to mediate redox sensing in many proteins [73]. To our knowledge, H-NOX is unique in that the zinc remains bound to the protein in a new coordination environment, although the precise binding site in the oxidized protein and its importance in HnoK inhibition remain unclear. Given the EXAFS data (Figure 4) and the results of mutagenesis near the zinc site, it is tempting to speculate that nearby His and Asp/Glu residues co-ordinate zinc in the oxidized state and are essential for stability. Unfortunately, a computational model corroborating this assertion could not be generated. This may be due to several reasons, including that (1) the initial homology H-NOX model could be not sufficiently accurate for the MD simulations and (2) the binding site in the oxidized protein is formed by slow conformational changes that could not be tracked with the microsecond-scale MD simulations.

Similarly, whether *Vc* H-NOX mediates biofilm formation in response to oxidative stress *in vivo* through this mechanism is uncertain. However, several studies have shown an increase of reactive oxygen species (ROS) in cholera patients relative to uninfected persons [74–76], and the expression of biofilm genes is important for various models of intestinal colonization [77–80]. Furthermore, biofilm-like aggregates of semi-dormant but infectious cells have been found in cholera patient stools and in the aquatic environment [81,82]. Thus, there does seem to be a relationship between biofilm formation and oxidative stress in *V. cholerae* similar to that confirmed in *Campylobacter jejuni* [83], another gut pathogen. It is possible that *Vc* H-NOX may play a role in redox sensing leading to biofilm formation, with potentially important implications on transmission and pathogenesis of cholera. Further studies will be required to evaluate this possibility.

In conclusion, we have confirmed and refined the mechanism of redox sensing by heme-free *Vc* H-NOX using experimental and computational tools. The results delineate the disulfide bonding pattern in the oxidized protein and confirm a dramatic change in zinc coordination environment. The overall conformational changes upon oxidation mimic those observed upon NO binding to the heme-bound protein and explain why cysteine oxidation results in HnoK inhibition. Given that the zinc-ligating Cys residues are conserved in several H-NOX homologs, it will be interesting to determine whether this mechanism is active in other members of the H-NOX family. Further experiments assessing this as well as the *in vivo* function of heme-independent redox signaling in H-NOX proteins promise to expand our understanding of the diversity of functions in this important sensor family.

Competing Interests

The authors declare that there are no competing interests associated with the manuscript.

Funding

This study was funded through startup funds from the Office of the Vice President for Research at New Mexico State University. Mass spectrometry instrumentation was purchased through NSF MRI#1626468 awarded to Dr. Tanner Schaub.

Author Contributions

R.M. and M.R.T. performed the computational aspects of the study. K.N.C. collected EXAFS data and performed all relevant analyses. J.M.J. collected mass spectrometry data. E.T.Y. prepared experimental samples and conceived the study. All authors contributed to writing the manuscript.

Acknowledgements

We gratefully acknowledge the use of facilities at the Stanford Synchrotron Radiation Lightsource, which is supported by the National Institutes of Health Biomedical Research and Technology Program Division of Research Resources and by the U.S. Department of Energy Office of Biological and Environmental Research. The computational resources were provided by the Extreme Science and Engineering Discovery Environment (XSEDE) TG-CHE170004. We further acknowledge Dr. Tanner Schaub, and the Center for Animal Health and Food Safety at NMSU for providing the mass spectrometry instrumentation.

Abbreviations

cMD, classical molecular dynamics; DW, Debye–Waller; ESI, electrospray ionization; EXAFS, extended X-ray absorption fine structure; FMO/DFTB3, fragment molecular orbital method/density functional tight binding; GB, generalized born; HCD, high collision-induced dissociation; HK, histidine kinases; H-NOX, heme nitric oxide/oxygen; HOCl, hypochlorous acid; MM/GBSA, molecular mechanics combined with generalized Born solvation surface area approach; MS³, mass spectrometry; NO, nitric oxide; PMF, potential of mean force; QM, quantum mechanical; RMSD, root-mean-square difference; sGC, soluble guanylate cyclase; SSN, sequence similarity network.

References

- 1 Iyer, L.M., Anantharaman, V. and Aravind, L. (2003) Ancient conserved domains shared by animal soluble guanylyl cyclases and bacterial signaling proteins. *BMC Genomics* **4**, 5 <https://doi.org/10.1186/1471-2164-4-5>
- 2 Lucas, K.A., Pitari, G.M., Kazerounian, S., Ruiz-Stewart, I., Park, J., Schulz, S. et al. (2000) Guanylyl cyclases and signaling by cyclic GMP. *Pharmacol. Rev.* **52**, 375–414 PMID: 10977868
- 3 Boon, E.M. and Marletta, M.A. (2005) Ligand specificity of H-NOX domains: from sGC to bacterial NO sensors. *J. Inorg. Biochem.* **99**, 892–902 <https://doi.org/10.1016/j.jinorgbio.2004.12.016>
- 4 Carlson, H.K., Vance, R.E. and Marletta, M.A. (2010) H-NOX regulation of c-di-GMP metabolism and biofilm formation in *Legionella pneumophila*. *Mol. Microbiol.* **77**, 930–942 <https://doi.org/10.1111/j.1365-2958.2010.07259.x>
- 5 Liu, N., Xu, Y., Hossain, S., Huang, N., Coursolle, D., Gralnick, J.A. et al. (2012) Nitric oxide regulation of cyclic di-GMP synthesis and hydrolysis in *Shewanella woodyi*. *Biochemistry* **51**, 2087–2099 <https://doi.org/10.1021/bi201753f>
- 6 Plate, L. and Marletta, M.A. (2012) Nitric oxide modulates bacterial biofilm formation through a multicomponent cyclic-di-GMP signaling network. *Mol. Cell* **46**, 449–460 <https://doi.org/10.1016/j.molcel.2012.03.023>
- 7 Kumar, S. and Spiro, S. (2017) Environmental and genetic determinants of biofilm formation in *Paracoccus denitrificans*. *mSphere* **2**, e00350-17 <https://doi.org/10.1128/mSphereDirect.00350-17>
- 8 Wang, Y., Dufour, Y.S., Carlson, H.K., Donohue, T.J., Marletta, M.A. and Ruby, E.G. (2010) H-NOX-mediated nitric oxide sensing modulates symbiotic colonization by *Vibrio fischeri*. *Proc. Natl. Acad. Sci. U.S.A.* **107**, 8375–8380 <https://doi.org/10.1073/pnas.1003571107>
- 9 Henares, B.M., Higgins, K.E. and Boon, E.M. (2012) Discovery of a nitric oxide responsive quorum sensing circuit in *Vibrio harveyi*. *ACS Chem. Biol.* **7**, 1331–1336 <https://doi.org/10.1021/cb300215t>
- 10 Price, M.S., Chao, L.Y. and Marletta, M.A. (2007) *Shewanella oneidensis* MR-1 H-NOX regulation of a histidine kinase by nitric oxide. *Biochemistry* **46**, 13677–13683 <https://doi.org/10.1021/bi7019035>
- 11 Mukhopadhyay, R., Sudasinghe, N., Schaub, T. and Yuki, E.T. (2016) Heme-independent redox sensing by the heme-nitric oxide/oxygen-binding protein (H-NOX) from *Vibrio cholerae*. *J. Biol. Chem.* **291**, 17547–17556 <https://doi.org/10.1074/jbc.M116.733337>
- 12 Wu, G., Liu, W., Berka, V. and Tsai, A.L. (2013) The selectivity of *Vibrio cholerae* H-NOX for gaseous ligands follows the “Sliding Scale Rule” hypothesis. Ligand interactions with both ferrous and ferric Vc H-NOX. *Biochemistry* **52**, 9432–9446 <https://doi.org/10.1021/bi401408x>
- 13 Herzik, Jr, M.A., Jonnalagadda, R., Kuriyan, J. and Marletta, M.A. (2014) Structural insights into the role of iron-histidine bond cleavage in nitric oxide-induced activation of H-NOX gas sensor proteins. *Proc. Natl. Acad. Sci. U.S.A.* **111**, E4156–E4164 <https://doi.org/10.1073/pnas.1416936111>
- 14 Consortium, U. (2019) Uniprot: a worldwide hub of protein knowledge. *Nucleic Acids Res.* **47**, D506–D515 <https://doi.org/10.1093/nar/gky1049>
- 15 Gerlt, J.A., Bouvier, J.T., Davidson, D.B., Imker, H.J., Sadkhin, B., Slater, D.R. et al. (2015) Enzyme Function Initiative-Enzyme Similarity Tool (EFI-EST): a web tool for generating protein sequence similarity networks. *Biochim. Biophys. Acta* **1854**, 1019–1037 <https://doi.org/10.1016/j.bbapap.2015.04.015>
- 16 Gerlt, J.A. (2017) Genomic enzymology: web tools for leveraging protein family sequence-function space and genome context to discover novel functions. *Biochemistry* **56**, 4293–4308 <https://doi.org/10.1021/acs.biochem.7b00614>

- 17 Zallot, R., Oberg, N.O. and Gerlt, J.A. (2018) ‘Democratized’ genomic enzymology web tools for functional assignment. *Curr. Opin. Chem. Biol.* **47**, 77–85 <https://doi.org/10.1016/j.cbpa.2018.09.009>
- 18 Shannon, P., Markiel, A., Ozier, O., Baliga, N.S., Wang, J.T., Ramage, D. et al. (2003) Cytoscape: a software environment for integrated models of biomolecular interaction networks. *Genome Res.* **13**, 2498–2504 <https://doi.org/10.1101/gr.1239303>
- 19 Sievers, F., Wilm, A., Dineen, D., Gibson, T.J., Karplus, K., Li, W. et al. (2011) Fast, scalable generation of high-quality protein multiple sequence alignments using Clustal Omega. *Mol. Syst. Biol.* **7**, 539 <https://doi.org/10.1038/msb.2011.75>
- 20 Waterhouse, A.M., Procter, J.B., Martin, D.M., Clamp, M. and Barton, G.J. (2009) Jalview Version 2—a multiple sequence alignment editor and analysis workbench. *Bioinformatics* **25**, 1189–1191 <https://doi.org/10.1093/bioinformatics/btp033>
- 21 Arnold, K., Bordoli, L., Kopp, J. and Schwede, T. (2006) The SWISS-MODEL workspace: a web-based environment for protein structure homology modelling. *Bioinformatics* **22**, 195–201 <https://doi.org/10.1093/bioinformatics/bti770>
- 22 Case, D.A., Cheatham, III, T.E., Darden, T., Gohlke, H., Luo, R., Merz, Jr, K.M. et al. (2005) The Amber biomolecular simulation programs. *J. Comput. Chem.* **26**, 1668–1688 <https://doi.org/10.1002/jcc.20290>
- 23 Maier, J.A., Martinez, C., Kasavajhala, K., Wickstrom, L., Hauser, K.E. and Simmerling, C. (2015) ff14SB: improving the accuracy of protein side chain and backbone parameters from ff99SB. *J. Chem. Theory Comput.* **11**, 3696–3713 <https://doi.org/10.1021/acs.jctc.5b00255>
- 24 Götz, A.W., Williamson, M.J., Xu, D., Poole, D., Le Grand, S. and Walker, R.C. (2012) Routine microsecond molecular dynamics simulations with AMBER on GPUs. 1. Generalized born. *J. Chem. Theory Comput.* **8**, 1542–1555 <https://doi.org/10.1021/ct200909j>
- 25 Salomon-Ferrer, R., Götz, A.W., Poole, D., Le Grand, S. and Walker, R.C. (2013) Routine microsecond molecular dynamics simulations with AMBER on GPUs. 2. Explicit solvent particle mesh Ewald. *J. Chem. Theory Comput.* **9**, 3878–3888 <https://doi.org/10.1021/ct400314y>
- 26 Essmann, U., Perera, L., Berkowitz, M.L., Darden, T., Lee, H. and Pedersen, L.G. (1995) A smooth particle mesh Ewald method. *J. Chem. Phys.* **103**, 8577–8593 <https://doi.org/10.1063/1.470117>
- 27 Jorgensen, W.L., Chandrasekhar, J., Madura, J.D., Impey, R.W. and Klein, M.L. (1983) Comparison of simple potential functions for simulating liquid water. *J. Chem. Phys.* **79**, 926–935 <https://doi.org/10.1063/1.445869>
- 28 Larsson, P., Hess, B. and Lindahl, E. (2011) Algorithm improvements for molecular dynamics simulations. *Wiley Interdiscip. Rev. Comput. Mol. Sci.* **1**, 93–108 <https://doi.org/10.1002/wcms.3>
- 29 Feenstra, K.A., Hess, B. and Berendsen, H.J.C. (1999) Improving efficiency of large time-scale molecular dynamics simulations of hydrogen-rich systems. *J. Comput. Chem.* **20**, 786–798 [https://doi.org/10.1002/\(SICI\)1096-987X\(199906\)20:8<786::AID-JCC5>3.0.CO;2-B](https://doi.org/10.1002/(SICI)1096-987X(199906)20:8<786::AID-JCC5>3.0.CO;2-B)
- 30 Harvey, M.J., Giupponi, G. and Fabritiis, G.D. (2009) ACEMD: Accelerating biomolecular dynamics in the microsecond time scale. *J. Chem. Theory Comput.* **5**, 1632–1639 <https://doi.org/10.1021/ct9000685>
- 31 Hopkins, C.W., Le Grand, S., Walker, R.C. and Roitberg, A.E. (2015) Long-time-step molecular dynamics through hydrogen mass repartitioning. *J. Chem. Theory Comput.* **11**, 1864–1874 <https://doi.org/10.1021/ct5010406>
- 32 Ryckaert, J.-P., Ciccott, G. and Berendsen, H.J.C. (1977) Numerical integration of the cartesian equations of motion of a system with constraints: molecular dynamics of n-alkanes. *J. Comput. Phys.* **23**, 327–341 [https://doi.org/10.1016/0021-9991\(77\)90098-5](https://doi.org/10.1016/0021-9991(77)90098-5)
- 33 Humphrey, W., Dalke, A. and Schulten, K. (1996) VMD: visual molecular dynamics. *J. Mol. Graph.* **14**, 33–38 [https://doi.org/10.1016/0263-7855\(96\)00018-5](https://doi.org/10.1016/0263-7855(96)00018-5)
- 34 Hawkins, G.D., Cramer, C.J. and Truhlar, D.G. (1996) Parametrized models of aqueous free energies of solvation based on pairwise descreening of solute atomic charges from a dielectric medium. *J. Phys. Chem.* **100**, 19824–19839 <https://doi.org/10.1021/jp961710n>
- 35 Hawkins, G.D., Cramer, C.J. and Truhlar, D.G. (1995) Pairwise solute descreening of solute charges from a dielectric medium. *Chem. Phys. Lett.* **246**, 122–129 [https://doi.org/10.1016/0009-2614\(95\)01082-K](https://doi.org/10.1016/0009-2614(95)01082-K)
- 36 Tsui, V. and Case, D.A. (2000) Theory and applications of the generalized Born solvation model in macromolecular simulations. *Biopolymers* **56**, 275–291 [https://doi.org/10.1002/1097-0282\(2000\)56:4<275::AID-BIP10024>3.0.CO;2-E](https://doi.org/10.1002/1097-0282(2000)56:4<275::AID-BIP10024>3.0.CO;2-E)
- 37 Torrie, G.M. and Valleau, J.P. (1977) Nonphysical sampling distributions in Monte Carlo free-energy estimation: Umbrella sampling. *J. Comput. Phys.* **23**, 187–199 [https://doi.org/10.1016/0021-9991\(77\)90121-8](https://doi.org/10.1016/0021-9991(77)90121-8)
- 38 Kumar, S., Rosenberg, J.M., Bouzida, D., Swendsen, R.H. and Kollman, P.A. (1992) THE weighted histogram analysis method for free-energy calculations on biomolecules. I. The method. *J. Comput. Chem.* **13**, 1011–1021 <https://doi.org/10.1002/jcc.540130812>
- 39 Dykstra, C., Frenking, G., Kim, K. and Scuseria, G. (2011) *Theory and Applications of Computational Chemistry*, Elsevier
- 40 Schmidt, M.W., Baldridge, K.K., Boatz, J.A., Elbert, S.T., Gordon, M.S., Jensen, J.H. et al. (1993) General atomic and molecular electronic structure system. *J. Comput. Chem.* **14**, 1347–1363 <https://doi.org/10.1002/jcc.540141112>
- 41 Fedorov, D.G., and Kitaura, K. (2006) Theoretical development of the fragment molecular orbital (FMO) method. In *Modern Methods for Theoretical Physical Chemistry of Biopolymers*, pp. 3–38, Elsevier
- 42 Fedorov, D.G. and Kitaura, K. (2007) Pair interaction energy decomposition analysis. *J. Comput. Chem.* **28**, 222–237 <https://doi.org/10.1002/jcc.20496>
- 43 Inadomi, Y., Nakano, T., Kitaura, K. and Nagashima, U. (2002) Definition of molecular orbitals in fragment molecular orbital method. *Chem. Phys. Lett.* **364**, 139–143 [https://doi.org/10.1016/S0009-2614\(02\)01291-5](https://doi.org/10.1016/S0009-2614(02)01291-5)
- 44 Kitaura, K., Ikeo, E., Asada, T., Nakano, T. and Uebayasi, M. (1999) Fragment molecular orbital method: an approximate computational method for large molecules. *Chem. Phys. Lett.* **313**, 701–706 [https://doi.org/10.1016/S0009-2614\(99\)00874-X](https://doi.org/10.1016/S0009-2614(99)00874-X)
- 45 Ishimoto, T., Tokiwa, H., Teramae, H. and Nagashima, U. (2005) Theoretical study of intramolecular interaction energies during dynamics simulations of oligopeptides by the fragment molecular orbital-Hamiltonian algorithm method. *J. Chem. Phys.* **122**, 094905 <https://doi.org/10.1063/1.1857481>
- 46 Suenaga, M. (2009) Facio Home Page, <http://zzfelis.sakura.ne.jp/index.html>
- 47 Fedorov, D.G., Kitaura, K., Li, H., Jensen, J.H. and Gordon, M.S. (2006) The polarizable continuum model (PCM) interfaced with the fragment molecular orbital method (FMO). *J. Comput. Chem.* **27**, 976–985 <https://doi.org/10.1002/jcc.20406>
- 48 Gandrud, C. (2016) *Reproducible Research with R and R Studio*, Chapman and Hall/CRC
- 49 Team RC. (2013) *R: a Language and Environment for Statistical Computing*, R Foundation for Statistical Computing, Vienna
- 50 Kluyver, T., Ragan-Kelley, B., Pérez, F., Granger, B.E., Bussonnier, M. Frederic, J. et al. (eds) (2016) Jupyter Notebooks—a publishing format for reproducible computational workflows. Computer Science, Published in ELPUB.
- 51 Ragan-Kelley, M., Perez, F., Granger, B., Kluyver, T., Ivanov, P. Frederic, J., et al. (eds) (2014) The Jupyter/IPython architecture: a unified view of computational research, from interactive exploration to communication and publication. AGU Fall Meeting Abstracts, Computer Science

- 52 George, G.N. (1995) *EXAFSPAK. A suite of computer programs for analysis of X-ray absorption spectra*. Stanford Synchrotron Radiation Laboratory, Menlo Park, USA
- 53 Binsted, N. and Hasnain, S.S. (1996) State-of-the-art analysis of whole X-ray absorption spectra. *J. Synchrotron. Radiat.* **3**(Pt 4), 185–196 <https://doi.org/10.1107/S0909049596005651>
- 54 Gurman, S.J., Binsted, N. and Ross, I. (1984) A rapid, exact curved-wave theory for EXAFS calculations. *J. Phys. C Solid State Phys.* **17**, 143–151 <https://doi.org/10.1088/0022-3719/17/1/019>
- 55 Gurman, S.J., Binsted, N. and Ross, I. (1986) A rapid, exact, curved-wave theory for EXAFS calculations. II. The multiple-scattering contributions. *J. Phys. C Solid State Phys.* **19**, 1845–1861 <https://doi.org/10.1088/0022-3719/19/11/021>
- 56 Pettersen, E.F., Goddard, T.D., Huang, C.C., Couch, G.S., Greenblatt, D.M., Meng, E.C. et al. (2004) UCSF chimera—a visualization system for exploratory research and analysis. *J. Comput. Chem.* **25**, 1605–1612 <https://doi.org/10.1002/jcc.20084>
- 57 Wu, S.L., Jiang, H., Lu, Q., Dai, S., Hancock, W.S. and Karger, B.L. (2009) Mass spectrometric determination of disulfide linkages in recombinant therapeutic proteins using online LC–MS with electron-transfer dissociation. *Anal. Chem.* **81**, 112–122 <https://doi.org/10.1021/ac801560k>
- 58 Mikesch, L.M., Ueberheide, B., Chi, A., Coon, J.J., Syka, J.E., Shabanowitz, J. et al. (2006) The utility of ETD mass spectrometry in proteomic analysis. *Biochim. Biophys. Acta* **1764**, 1811–1822 <https://doi.org/10.1016/j.bbapap.2006.10.003>
- 59 Clark, D.F., Go, E.P. and Desaire, H. (2013) Simple approach to assign disulfide connectivity using extracted ion chromatograms of electron transfer dissociation spectra. *Anal. Chem.* **85**, 1192–1199 <https://doi.org/10.1021/ac303124w>
- 60 McLafferty, F.W., Horn, D.M., Breuker, K., Ge, Y., Lewis, M.A., Cerda, B. et al. (2001) Electron capture dissociation of gaseous multiply charged ions by Fourier-transform ion cyclotron resonance. *J. Am. Soc. Mass Spectrom.* **12**, 245–249 [https://doi.org/10.1016/S1044-0305\(00\)00223-3](https://doi.org/10.1016/S1044-0305(00)00223-3)
- 61 Loo, J.A., Edmonds, C.G., Udseth, H.R. and Smith, R.D. (1990) Effect of reducing disulfide-containing proteins on electrospray ionization mass spectra. *Anal. Chem.* **62**, 693–698 <https://doi.org/10.1021/ac00206a009>
- 62 Wang, Y., Lu, Q., Wu, S.L., Karger, B.L. and Hancock, W.S. (2011) Characterization and comparison of disulfide linkages and scrambling patterns in therapeutic monoclonal antibodies: using LC–MS with electron transfer dissociation. *Anal. Chem.* **83**, 3133–3140 <https://doi.org/10.1021/ac200128d>
- 63 Cole, S.R., Ma, X., Zhang, X. and Xia, Y. (2012) Electron transfer dissociation (ETD) of peptides containing intrachain disulfide bonds. *J. Am. Soc. Mass Spectrom.* **23**, 310–320 <https://doi.org/10.1007/s13361-011-0300-z>
- 64 Guan, X., Zhang, L. and Wypych, J. (2018) Direct mass spectrometric characterization of disulfide linkages. *MAbs* **10**, 572–582 <https://doi.org/10.1080/19420862.2018.1442998>
- 65 Guo, Y. and Marletta, M.A. (2019) Structural insight into H-NOX gas sensing and cognate signaling protein regulation. *ChemBiochem* **20**, 7–19 <https://doi.org/10.1002/cbic.201800478>
- 66 Erbil, W.K., Price, M.S., Wemmer, D.E. and Marletta, M.A. (2009) A structural basis for H-NOX signaling in *Shewanella oneidensis* by trapping a histidine kinase inhibitory conformation. *Proc. Natl. Acad. Sci. U.S.A.* **106**, 19753–19760 <https://doi.org/10.1073/pnas.0911645106>
- 67 Pellicena, P., Karow, D.S., Boon, E.M., Marletta, M.A. and Kuriyan, J. (2004) Crystal structure of an oxygen-binding heme domain related to soluble guanylate cyclases. *Proc. Natl. Acad. Sci. U.S.A.* **101**, 12854–9 <https://doi.org/10.1073/pnas.0405188101>
- 68 Hespen, C.W., Bruegger, J.J., Phillips-Piro, C.M. and Marletta, M.A. (2016) Structural and functional evidence indicates selective oxygen signaling in *Caldanaerobacter subterraneus* H-NOX. *ACS Chem. Biol.* **11**, 2337–2346 <https://doi.org/10.1021/acscchembio.6b00431>
- 69 Olea, C., Boon, E.M., Pellicena, P., Kuriyan, J. and Marletta, M.A. (2008) Probing the function of heme distortion in the H-NOX family. *ACS Chem. Biol.* **3**, 703–710 <https://doi.org/10.1021/cb800185h>
- 70 Olea C, J., Herzik MA, J., Kuriyan, J. and Marletta, M.A. (2010) Structural insights into the molecular mechanism of H-NOX activation. *Protein Sci.* **19**, 881–887 <https://doi.org/10.1002/pro.357>
- 71 Rao, M., Herzik, M.A., Iavarone, A.T. and Marletta, M.A. (2017) Nitric oxide-induced conformational changes govern H-NOX and histidine kinase interaction and regulation in *Shewanella oneidensis*. *Biochemistry* **56**, 1274–1284 <https://doi.org/10.1021/acs.biochem.6b01133>
- 72 Guo, Y., Iavarone, A.T., Cooper, M.M. and Marletta, M.A. (2018) Mapping the H-NOX/HK binding interface in *Vibrio cholerae* by hydrogen/deuterium exchange mass spectrometry. *Biochemistry* **57**, 1779–1789 <https://doi.org/10.1021/acs.biochem.8b00027>
- 73 Cremers, C.M. and Jakob, U. (2013) Oxidant sensing by reversible disulfide bond formation. *J. Biol. Chem.* **288**, 26489–26496 <https://doi.org/10.1074/jbc.R113.462929>
- 74 Bhattacharyya, S., Ghosh, S., Shant, J., Ganguly, N.K. and Majumdar, S. (2004) Role of the W07-toxin on *Vibrio cholerae*-induced diarrhoea. *Biochim. Biophys. Acta* **1670**, 69–80 <https://doi.org/10.1016/j.bbagen.2003.10.016>
- 75 Qadri, F., Raqib, R., Ahmed, F., Rahman, T., Wenneras, C., Das, S.K. et al. (2002) Increased levels of inflammatory mediators in children and adults infected with *Vibrio cholerae* O1 and O139. *Clin. Diagn. Lab. Immunol.* **9**, 221–229 <https://doi.org/10.1128/cdli.9.2.221-229.2002>
- 76 Ellis, C.N., LaRocque, R.C., Uddin, T., Krastins, B., Mayo-Smith, L.M., Sarracino, D. et al. (2015) Comparative proteomic analysis reveals activation of mucosal innate immune signaling pathways during cholera. *Infect Immun.* **83**, 1089–1103 <https://doi.org/10.1128/IAI.02765-14>
- 77 Xu, Q., Dziejman, M. and Mekalanos, J.J. (2003) Determination of the transcriptome of *Vibrio cholerae* during intrainestinal growth and midexponential phase in vitro. *Proc. Natl. Acad. Sci. U.S.A.* **100**, 1286–1291 <https://doi.org/10.1073/pnas.0337479100>
- 78 Fong, J.C., Syed, K.A., Klose, K.E. and Yildiz, F.H. (2010) Role of *Vibrio* polysaccharide (vps) genes in VPS production, biofilm formation and *Vibrio cholerae* pathogenesis. *Microbiology* **156**(Pt 9), 2757–2769 <https://doi.org/10.1099/mic.0.040196-0>
- 79 Blow, N.S., Salomon, R.N., Garrity, K., Reveillaud, I., Kopin, A., Jackson, F.R. et al. (2005) *Vibrio cholerae* infection of *Drosophila melanogaster* mimics the human disease cholera. *PLoS Pathog.* **1**, e8 <https://doi.org/10.1371/journal.ppat.0010008>
- 80 Purdy, A.E. and Watnick, P.I. (2011) Spatially selective colonization of the arthropod intestine through activation of *Vibrio cholerae* biofilm formation. *Proc. Natl. Acad. Sci. U.S.A.* **108**, 19737–19742 <https://doi.org/10.1073/pnas.1111530108>
- 81 Faruque, S.M., Islam, M.J., Ahmad, Q.S., Faruque, A.S., Sack, D.A., Nair, G.B. et al. (2005) Self-limiting nature of seasonal cholera epidemics: Role of host-mediated amplification of phage. *Proc. Natl. Acad. Sci. U.S.A.* **102**, 6119–6124 <https://doi.org/10.1073/pnas.0502069102>
- 82 Faruque, S.M., Biswas, K., Udden, S.M., Ahmad, Q.S., Sack, D.A., Nair, G.B. et al. (2006) Transmissibility of cholera: in vivo-formed biofilms and their relationship to infectivity and persistence in the environment. *Proc. Natl. Acad. Sci. U.S.A.* **103**, 6350–6355 <https://doi.org/10.1073/pnas.0601277103>
- 83 Oh, E., Kim, J.C. and Jeon, B. (2016) Stimulation of biofilm formation by oxidative stress in *Campylobacter jejuni* under aerobic conditions. *Virulence* **7**, 846–851 <https://doi.org/10.1080/21505594.2016.1197471>